

DIFFERENTIAL MICROLENSING OF THE CONTINUUM AND BROAD EMISSION LINES IN SDSS J0924+0219, THE MOST ANOMALOUS LENSED QUASAR*

CHARLES R. KEETON¹, SCOTT BURLES², PAUL L. SCHECHTER², AND JOACHIM WAMBSGANSS³

Accepted in ApJ

ABSTRACT

SDSS J0924+0219 is the most glaring example of a gravitational lens with anomalous flux ratios: optical broad-band photometry shows image D to be a factor of 12 fainter than expected for smooth lens potentials. We report spectroscopy showing that the anomaly is present in the broad emission line flux ratios as well. There are differences between the emission line and continuum flux ratios: the A/D ratio is 10 in the broad Lyman- α line and 19 in the associated continuum. Known variability argues for the presence of microlensing. We show that microlensing can account for both the continuum and emission line flux ratios, if the broad emission line region is comparable in size to the Einstein radii of the microlenses. Specifically, we need the half-light radius of the broad-line region to be $R_{\text{BLR}} \lesssim 0.4 R_E \sim 9$ lt-days, which is small but reasonable. If the broad-line region is that large, then stars can contribute only 15–20% of the surface mass density at the positions of the images. While we cannot exclude the possibility that millilensing by dark matter substructure is present as well, we conclude that microlensing is present and sufficient to explain existing data. Under this hypothesis, the A/D flux ratio should return to a value close to unity on a time scale of years rather than millennia.

Subject headings: cosmology: theory — gravitational lensing — quasars: individual (SDSS J0924+0219)

1. INTRODUCTION

The gravitational lens system SDSS J0924+0219 presents a fascinating challenge for lens modelers. Discovered by Inada et al. (2003), images from the Sloan Digital Sky Survey showed what appeared to be a triple system in a very odd configuration. The lensing galaxy could be seen in higher resolution follow-up observations obtained with the Baade telescope at Las Campanas Observatory, which in combination with the three known images called for a fourth image. Modeling and subtracting the three bright images (A, B, and C) did reveal a fourth image, D, but it was a factor of 10 fainter than predicted. The image positions are typical of an “inclined quad” or “fold” configuration produced by a source near a fold caustic (see Saha & Williams 2003), so images A and D ought to be nearly equal in brightness (see Keeton et al. 2005).

Anomalies in lens flux ratios are possible when there is small-scale structure in the lensing galaxy, in the form of either dark matter subhalos (millilensing; e.g., Mao & Schneider 1998; Metcalf & Madau 2001; Chiba 2002; Dalal & Kochanek 2002) or stars (microlensing; e.g., Chang & Refsdal 1979; Schechter & Wambsganss 2002). The challenge is to understand whether either possibility can actually explain why image D is so faint. One might hope to discriminate between milli- and microlensing by observing a component of the QSO that is large compared to the Einstein rings of stars but small compared to the Einstein rings of subhalos (Moustakas & Metcalf 2003; Wisotzki et al. 2003; Metcalf et al. 2004; Chiba et al. 2005; Wayth et al. 2005). We therefore obtained broad emission line flux ratios for SDSS

J0924+0219 using the Hubble Space Telescope. We describe our observations in §2, our analysis in §3, and our conclusions in §4. We assume a cosmology with $\Omega_M = 0.3$, $\Omega_\Lambda = 0.7$, and $H_0 = 70 \text{ km s}^{-1} \text{ Mpc}^{-1}$. The redshift of the source quasar is $z_s = 1.524$ (Inada et al. 2003), and the redshift of the lens galaxy is $z_l = 0.394$ (Eigenbrod et al. 2005).

2. OBSERVATIONS

2.1. Imaging

SDSS0924 was observed with the Wide Field Channel (WFC) of the Advanced Camera for Surveys (ACS) on the Hubble Space Telescope, as part of program GO-9744 (PI C. Kochanek). Four 547-sec exposures were obtained with the F555W filter ($\approx V$) on 18 November 2003, and four 574-sec exposures were obtained with the F814W ($\approx I$) on 19 November 2003. An interpolated color composite of the V- and I-band images is shown in Figure 1a. The four QSO components and the lens galaxy are clearly visible. An Einstein ring image of the QSO host galaxy is also apparent in the I-band image.

We performed a non-linear least squares fit to the flattened frames from standard ACS data processing, using a photometric model consisting of four point sources and a de Vaucouleurs model galaxy, convolved with a TinyTim PSF (Krist 1995, v6.2). We fit each exposure separately and used the scatter among exposures to assess the measurement uncertainties. For the galaxy we find an I-band effective radius $R_{\text{eff}} = 0''.436 \pm 0''.004$, an axis ratio $q = 0.92 \pm 0.02$, and a position angle $\theta_q = -25^\circ \pm 5^\circ$ (East of North). The positions and broad-band fluxes of the QSO components are listed in Table 1. The HST flux ratios are consistent with those reported by Inada et al. (2003).

2.2. Spectroscopy

We planned for SDSS0924 to be observed as the final and most important target in our HST program GO-9854 to obtain spatially resolved spectroscopy of eight quadruply lensed systems with the Space Telescope Imaging Spectrograph (STIS).

*BASED ON OBSERVATIONS MADE WITH THE NASA/ESA HUBBLE SPACE TELESCOPE, OBTAINED AT THE SPACE TELESCOPE SCIENCE INSTITUTE, WHICH IS OPERATED BY AURA, INC., UNDER NASA CONTRACT NAS 5-26555.

¹ Department of Physics & Astronomy, Rutgers University, Piscataway, NJ 08837 USA

² Kavli Institute for Astrophysics and Space Research and Department of Physics, Massachusetts Institute of Technology, Cambridge, MA 02139 USA

³ Astronomisches Rechen-Institut, Zentrum für Astronomie, Universität Heidelberg, Mönchhofstrasse 12-14, 69120 Heidelberg, Germany

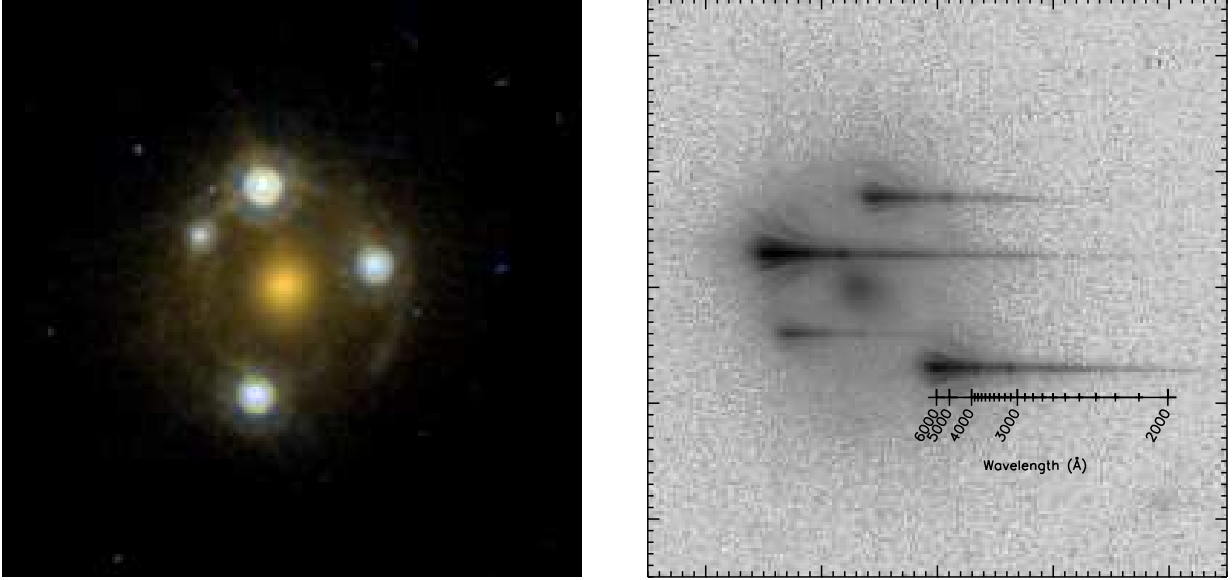


FIG. 1.— Direct ACS/WFC (left) and dispersed ACS/HRC (right) $5'' \times 5''$ images of SDSS J0924+0219 from the Hubble Space Telescope. The direct image is oriented with North up and East to the left. Clockwise from the top, the quasar components are labeled A, C, B, and D. The dispersed image is rotated by $\sim 70^\circ$. Each image is displayed with a non-linear stretch given by an inverse hyperbolic sine to highlight both bright and faint features. An approximate wavelength scale is superposed on the dispersed image to show the effective wavelength solution.

TABLE 1. COMPONENT POSITIONS AND FLUXES OF SDSS J0924+0219

Image	$-\Delta\alpha$ (")	$\Delta\delta$ (")	σ (")	F_I	F_V	F_{17}	F_{12}	F_α
A	0.0000	0.0000	0.0010	529.5 ± 3.2	274.9 ± 2.5	5.59	2.49	120.3
B	-0.0636	-1.8063	0.0010	246.4 ± 2.1	141.8 ± 0.7	1.66	0.66	46.2
C	0.9648	-0.6788	0.0013	181.3 ± 0.7	106.7 ± 1.5	0.62	0.24	21.6
D	-0.5414	-0.4296	0.0026	36.7 ± 0.5	16.9 ± 0.6	0.29	0.10	11.8
G	0.1804	-0.8685	0.0039	376.8 ± 1.5	61.3 ± 2.9			

NOTE. — F_I and F_V are broad-band fluxes in the HST I and V bands, respectively, expressed in counts per second. The uncertainties derived from the scatter among exposures are consistent with Poisson noise. These fluxes can be converted to AB magnitudes using zeropoints of 25.937 in I and 25.718 in V. F_{17} and F_{12} are spectroscopic continuum fluxes at rest wavelengths of 1700 Å and 1216 Å, respectively, in units of 10^{-17} ergs cm^{-2} s^{-1} Å $^{-1}$. Component D has a systematic uncertainty of $\sim 20\%$ in F_{12} due to galaxy subtraction (see text). F_α is the flux in the Ly α /N V broad emission line, in units of 10^{-17} ergs cm^{-2} s^{-1} .

The observations were attempted on 19 June 2004, but guide star acquisition failed. We arranged to reobserve SDSS0924 with the same setup, but the power supply to STIS was shut down before the new observations were carried out.

We considered whether ACS could be used to conduct the desired observations, and realized that the sapphire prism (PR200L) in the High Resolution Channel (HRC) of ACS would provide coverage of the broad emission lines of Lyman- α , Si IV and C IV. The observations were successfully executed on 29 May 2005. The combined image of three 880-sec exposures is shown in Figure 1b. The visible and near-UV light from 6000 Å to 2000 Å is dispersed over 80 native HRC pixels. The dispersion per pixel ranges from 14000 km s^{-1} at 6000 Å to 4000 km s^{-1} at 3000 Å to 1300 km s^{-1} at 2000 Å.

The combined cosmic ray rejected product from STScI provided the starting point for spectral extraction. We subtracted the galaxy by masking the dispersed footprints of the four QSO images and modeling the galaxy surface brightness distribution with a linear b-spline model (cf. Bolton et al. 2005). The relative wavelength was given by the ground calibration of ACS (Pavlovsky et al. 2004), and we shifted the wavelength scale of each spectrum to match the obvious emission features (Ly α /N V, Ly β /O VI, C IV) present in the QSO dispersed images. The spectrum of each QSO image was con-

structed by a simple boxcar extraction in each column with a boxcar half-width in pixels given by $\sqrt{\lambda}/24$. The count rate in each spectral pixel was converted to flux using sensitivity tables produced from ground calibrations. The extracted spectra are shown in Figure 2.

We fit a simple five parameter model composed of a linear continuum and a Gaussian emission line to each spectrum over the range 1120–1460 Å in the QSO frame, covering the Ly α /N V broad emission line. The fits are shown in Figure 2, and the line and continuum fluxes are listed in Table 1 as F_α and F_{12} , respectively. We also report the average continuum flux level over the rest wavelength range 1600–1800 Å as F_{17} .

Figure 1b shows that the spectra for images A and D pass fairly close to the center of the galaxy. To assess systematic effects due to the galaxy subtraction, we repeated the measurements with both 5% more and less galaxy subtracted. All of the spectral flux measurements in Table 1 varied by less than 5%, with the exception of the continuum measurement F_{12} for image D which varied by 20%. One other possible systematic effect is that F_{17} may contain a small amount ($\lesssim 5\%$) of broad line flux, but that should not affect our conclusions.

2.3. Comments

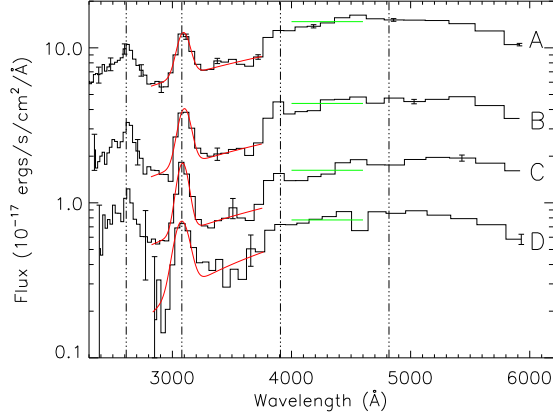


FIG. 2.— Extracted spectra of the four images, versus observed wavelength. Sample errorbars are shown only in certain bins for clarity. The vertical lines indicate the expected locations of the broad emission line complexes Ly β /O VI, Ly α /N V, C IV, and C III], given the quasar redshift $z_s = 1.524$ (Inada et al. 2003); they provide an external check on our wavelength solutions. The red curves show our models of Gaussian emission lines at Ly α /N V, with linear continua, fit to each spectrum over the rest wavelength range 1120–1460 Å. The green lines indicate the average continuum levels over the rest wavelength range 1600–1800 Å.

SDSS0924 is anomalous not just in broad-band photometry but also in the continuum and broad emission line flux ratios. Moreover, the anomalies are different in different passbands: A/D is 10 in the emission line, 14–16 in the broad-band filters, and >19 in the continuum. That the broad-band values lie between the emission line and continuum values makes sense if the broad-band filters contain both continuum and emission line light. (We estimate that $\sim 10\%$ of the V-band flux is from broad emission lines, while the I-band contains $\sim 20\%$ emission line flux including the 3000 Å bump.) For comparison, the values for A/C are 5.6 in the emission line, 2.6–2.9 in the broad-band filters, and >9 in the continuum. That the broad-band values lie below both the emission line and continuum values may seem puzzling. However, we must recall that the photometry and spectroscopy come from different epochs, and image C has faded since November 2003 (Kochanek 2004) such that the broad-band ratio is presently A/C ~ 5 .

3. ANALYSIS

3.1. Basic picture

Optical broad-band photometry shows that the images vary independently and on a time scale of years (Kochanek 2004), which is long compared with the predicted time delays (see §3.2) and therefore implies that microlensing is present. Microlensing can also explain why the emission line and continuum flux ratios differ, as we shall demonstrate (also see Schneider & Wambsganss 1990; Metcalf et al. 2004; Wayth et al. 2005).

What remains is to explain why the emission line flux ratios are anomalous. We initially suspected millilensing, but then realized that we would need at least two clumps since both C and D have anomalous emission line flux ratios. Since we know that microlensing is present, a simpler hypothesis is that microlensing produces all of the anomalies. We will show that microlensing can indeed explain the data for SDSS0924.

One obvious question is whether microlensing has the right scale to affect broad emission lines. The source plane Einstein

radius of a star of mass M is

$$R_E = \left(\frac{4GM}{c^2} \frac{D_{ls}D_{os}}{D_{ol}} \right)^{1/2} \approx 22 \left(\frac{M}{M_\odot} \right)^{1/2} \text{ lt-days}. \quad (1)$$

For comparison, reverberation mapping studies have shown that the broad line regions of active galactic nuclei span a range of sizes but certainly extend down to ~ 10 lt-days and below (e.g., Kaspi et al. 2005, and references therein). The comparison is not perfect because reverberation mapping studies have focused on Balmer lines (especially H β) while we have observed Ly α , and because reverberation mapping and microlensing are probably sensitive to source geometry in different ways. Nevertheless, it appears that the microlensing scale is not grossly inappropriate.

3.2. Macromodel

For a microlensing analysis we need to estimate the convergence and shear at the position of each image. We treat the lens galaxy as a singular isothermal ellipsoid whose surface mass density (in units of the critical density for lensing) can be written as

$$\frac{\Sigma(r, \theta)}{\Sigma_{\text{crit}}} = \frac{b}{2r} \left[\frac{1+q^2}{(1+q^2) - (1-q^2)\cos 2(\theta-\theta_q)} \right]^{1/2}, \quad (2)$$

where q is the projected axis ratio, θ_q is the orientation angle, and b is a mass parameter related to the Einstein radius of the lens. We constrain the center of the mass distribution using the observed galaxy position. We optimize b and q , but fix θ_q to match the orientation of the observed galaxy (see Kochanek 2002). We include an external tidal shear to allow for the possibility that the environment of the lens galaxy (which is currently unknown) affects the lens potential (e.g., Keeton et al. 1997).

We fit the image and galaxy positions (not the flux ratios, since they are the subject of the microlensing analysis). The best-fit model has $\chi^2 = 33$ for $\nu = 2$ degrees of freedom, which is dominated by the galaxy position suggesting that we may have underestimated its uncertainty. (Eliminating the galaxy position constraint leads to $\chi^2 = 2$.) Allowing the orientation to be free would yield $\chi^2 = 15$ for $\nu = 1$, again dominated by the galaxy position, but this model has a misalignment of 48° between the mass and the light so we deem it to be implausible.

The model has an axis ratio $q_{\text{mod}} = 0.81$, which is not very different from the observed axis ratio $q_{\text{obs}} = 0.92$. It has an external shear $\gamma_{\text{ext}} = 0.10$ at position angle $\theta_{\text{ext}} = 71^\circ$ (East of North); such a shear is typical for four-image lenses and suggests that the lens may lie in a modest group of galaxies (e.g., Momcheva et al. 2005). The predicted convergence κ , shear γ , and magnification μ for each image are listed in Table 2. The predicted time delays between the images are all less than 12 days. Thus, independent variability in the images on a time scale of years cannot be attributed to intrinsic variability of the source.

3.3. Toy microlensing

A toy model for microlensing features a single star that is nearly aligned with one of the lensed images. The image will be split into several “microimages” separated by a distance comparable to the star’s Einstein radius R_E . On this tiny scale the effects of the galaxy can be approximated as a constant convergence κ and shear γ , so that the lens equation can be

TABLE 2. MACROMODEL PROPERTIES

Image	κ	γ	μ
A	0.502	0.458	26.2
B	0.503	0.405	12.0
C	0.511	0.560	-13.4
D	0.476	0.565	-22.4

written as

$$u = x \left(1 - \kappa - \gamma - \frac{R_E^2}{x^2 + y^2} \right), \quad (3)$$

$$v = y \left(1 - \kappa + \gamma - \frac{R_E^2}{x^2 + y^2} \right), \quad (4)$$

in coordinates centered on the star and aligned with the shear. For a point source, the magnification of a microimage at (x, y) is

$$\mu(x, y) = \left\{ (1 - \kappa)^2 - \gamma^2 - \frac{R_E^2 [R_E^2 - 2\gamma(x^2 - y^2)]}{(x^2 + y^2)^2} \right\}^{-1}. \quad (5)$$

Suppose the star is perfectly aligned with the macroimage, so $u = v = 0$. Consider a negative-parity macroimage, such that $1 - \kappa - \gamma < 0$ and $1 - \kappa + \gamma > 0$. Then the lens equation is easily solved to find that there are two microimages at $x = 0$ and $y = \pm R_E / \sqrt{1 - \kappa + \gamma}$, and each has magnification $\mu = -1/[4\gamma(1 - \kappa + \gamma)]$.⁴ Since the microimages are not separately resolved, what matters is the combined magnification $\mu_{\text{tot}} = 1/[2\gamma(1 - \kappa + \gamma)]$ (also see Schechter & Wambsganss 2002). Using the convergence and shear values from Table 2 yields $\mu_{\text{tot}} = -0.813$, which corresponds to a flux ratio $D/A = 0.031$.

For imperfect alignment, we can still solve the lens equation analytically if the source lies on the u -axis or v -axis (see Appendix B.1 of Keeton et al. 2003 for details). For a source lying a distance $d < R_E$ from the origin along either axis, we find $D/A = 0.031 + 0.027(d/R_E)^2 + \mathcal{O}(d/R_E)^4$.

Clearly microlensing can cause image D to be very faint, if there is a star reasonably close to the macroimage.

3.4. Realistic microlensing

Going beyond the toy model, we face three important questions: (1) When the density of stars is low (so their caustics do not intersect), how likely is it that there is a star close enough to the macroimage to produce strong flux perturbations? (2) As the density of stars increases (so their caustics merge), is it still possible to get a strong demagnification? (3) How do the conclusions differ for point-like and finite sources?

To answer these questions, we run microlensing simulations using the ray shooting software by Wambsganss (1990a,b, 1999). We use the convergences and shears from Table 2, and assume that a fraction f_* of the surface mass density is in stars. The software produces a magnification map for each image. Treating the continuum region as a point source, we can make a histogram of the magnifications in the map to obtain the probability distribution for the continuum magnification. Given a model of the broad line region, we can convolve the magnification map with that model before making the histogram to obtain the probability distribution for the emission

⁴ If the macroimage has positive parity (such that $1 - \kappa + \gamma > 1 - \kappa - \gamma > 0$), there are two additional microimages at $x = \pm R_E / \sqrt{1 - \kappa - \gamma}$ and $y = 0$, each having magnification $\mu = 1/[4\gamma(1 - \kappa - \gamma)]$.

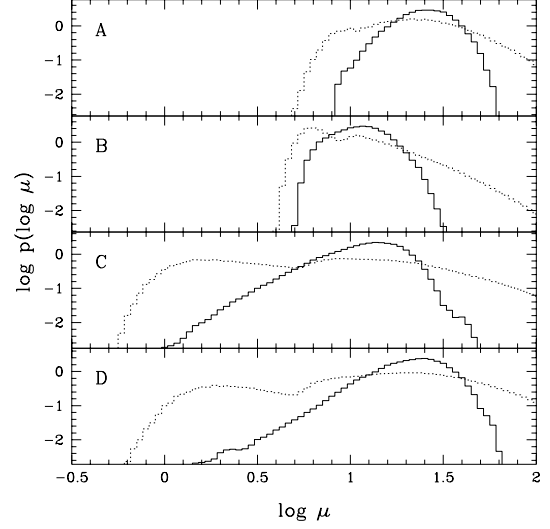


FIG. 3.— Microlensing magnification distributions for the four images of SDSS0924, assuming $f_* = 15\%$ of the surface mass density is in stars. The dotted histograms show the distributions for the continuum, assuming it to be a point source. The solid histograms show the results for the emission lines, assuming the broad line region to be a Gaussian with a half-light radius $R_{\text{BLR}}/R_E = 0.4$.

line magnification. We treat the BLR as a Gaussian with half-light radius R_{BLR} , since Mortonson et al. (2005) argue that details other than the half-light radius do not significantly affect microlensing magnification distributions. Examples of the distributions are shown in Figure 3.

To analyze both continuum and emission line flux ratios, we must determine the joint probability distribution $p(\mu_c, \mu_l)$ for the continuum and emission line magnifications of each image. For each source position, we take μ_c from the raw magnification map and μ_l from the convolved map, and then use all pixels to construct a histogram in the (μ_c, μ_l) plane.

Finally, to simultaneously analyze images A and D we compute the four-dimensional probability distribution⁵

$$p(\boldsymbol{\mu}) = p_A(\mu_c^A, \mu_l^A) \times p_D(\mu_c^D, \mu_l^D). \quad (6)$$

This represents the probability density for image A to have continuum and emission line magnifications of μ_c^A and μ_l^A , respectively, while image D has μ_c^D and μ_l^D . The joint four-dimensional distribution is just the product of the two two-dimensional distributions because microlensing is independent in the two images.

To quantify microlensing's ability to explain our data for SDSS0924, we then compute

$$P = \int d\boldsymbol{\mu} p(\boldsymbol{\mu}) \times \begin{cases} 1 & \mu_c^A/\mu_c^D \geq 19 \text{ and } \mu_l^A/\mu_l^D \geq 10 \\ 0 & \text{else} \end{cases} \quad (7)$$

This represents the probability that, if we picked a four-image lens at random, it would be at least as anomalous as what we have observed.

This is not really the right figure of merit for evaluating our data, though, because we did not select SDSS0924 at random; we chose it specifically because it is the most anomalous of the 22 known four-image lenses. A better figure of merit is the probability P_N of finding at least one strong anomaly in a

⁵ To simplify the notation, we collect the four magnifications into the vector $\boldsymbol{\mu} = (\mu_c^A, \mu_l^A, \mu_c^D, \mu_l^D)$.

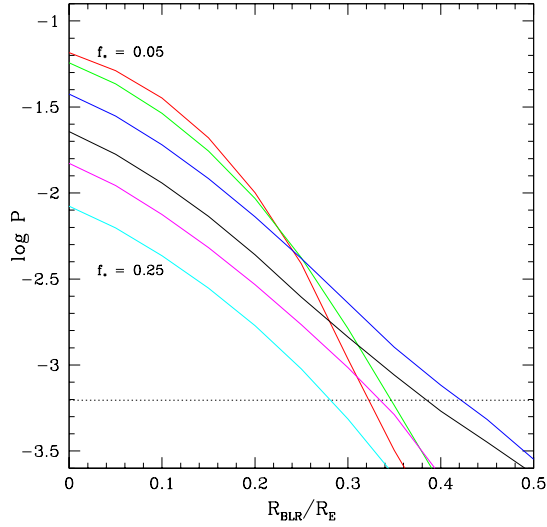


FIG. 4.— Logarithm of the P -value, or the probability of having a flux ratio anomaly more extreme than observed, as a function of the half-light radius of the broad line region. Each curve has a fixed value of the stellar mass fraction f_* ; at left, the curves are in order $f_* = 0.05, 0.10, 0.15, 0.20, 0.25$ from top to bottom. The dotted line shows our nominal acceptability threshold $P = 6.25 \times 10^{-4}$.

sample of N four-image lenses. Unfortunately, it is not clear how to compute P_N . For N identical lenses, the binomial distribution would give $P_N = 1 - (1 - P)^N \approx NP$ (for $P \ll 1$). The known lenses are not identical, but short of doing microlensing simulations for all of them (interesting, certainly, but beyond the scope of this work) we must assume that the value of P for SDSS0924 is representative. Next, we must determine an appropriate value for N . There are 16 four-image lenses with “fold” or “cusp” configurations, in which a close pair or triplet of images can be analyzed in a robust, model-independent way to find flux ratio anomalies (Keeton et al. 2003, 2005). We therefore set $N = 16$, and consider this to be somewhat conservative since we are neglecting the non-fold/cusp images in these 16 lenses as well as all images in the six known “cross” lenses. Lastly, we must decide what value of P_N represents a reasonable threshold of acceptability. Since we are dealing with complicated posterior probabilities we should avoid being too demanding, so we believe it is reasonable to consider $P_N = 1\%$, or $P \approx 0.01/16 \approx 6.25 \times 10^{-4}$.

Figure 4 shows P as a function of the half-light radius of the broad-line region, for different values of the stellar mass fraction f_* . There are acceptable models with the BLR as large as $R_{\text{BLR}}/R_E \sim 0.4$, for a stellar mass fraction of $f_* \sim 15\text{--}20\%$. A larger broad-line region is ruled out by these models. A smaller broad-line region would allow a wider range of stellar mass fractions. Thus, we conclude that there is a range of microlensing models with reasonable parameters that can explain the flux ratio anomaly in SDSS0924 acceptably well.

There are two limitations to our present analysis. First, we assumed for simplicity that the stellar mass fraction is the same for images A and D. Second, we assumed that all the stars have the same mass. The stellar mass function has very little effect on the magnification distribution for a point source (see Schechter et al. 2004, and references therein). The same result cannot hold for an extended source, because a large source must not be sensitive to stars that are sufficiently small,

but the problem of microlensing of a finite source by unequal-mass stars has not yet been studied. Relaxing our two assumptions should only make it *easier* to find microlensing models that fit the data, which means that they do not affect our main conclusion that microlensing can provide a reasonable explanation for SDSS0924.

4. DISCUSSION

We have discovered that the continuum and broad emission line flux ratios in SDSS0924 differ from each other at the factor of two level (for both images C and D). That fact, together with photometric variability (Kochanek 2004), establishes that microlensing is present in this system. We have also found that image D is highly anomalous in both the continuum and the broad emission line fluxes. We have shown that all of these results can be explained by microlensing.

The key point is that saddle images can be strongly suppressed by microlensing. The suppression is generally greater for a point source than for an extended source, which is why images C and D are fainter (relative to A) in the continuum than in the emission line. Even so, microlensing can produce a factor of 10 suppression in the emission line flux of image D, provided that the QSO broad emission line region has a half-light radius $R_{\text{BLR}} \lesssim 0.4 R_E \sim 9$ lt-days. While this result suggests that R_{BLR} is smaller than we thought broad-line regions to be when we began our project (also see Moustakas & Metcalf 2003), it seems reasonable in light of results from reverberation mapping of active galactic nuclei (e.g., Kaspi et al. 2005). That is all we can say without a detailed understanding of geometric factors that may make sizes measured from microlensing different from those measured by reverberation mapping. But it is enough for our proof of principle that microlensing is sufficient to explain all current data for SDSS0924.

We believe that microlensing offers the best and most natural explanation for SDSS0924, but concede that we cannot rigorously rule millilensing out. Testing whether millilensing is present will require new data, such as flux ratios in narrow emission lines (the narrow line region is generally thought to be large; e.g., Kraemer et al. 1998; but see Bennert et al. 2002 for a contrasting view) or mid-infrared photometry (e.g., Chiba et al. 2005). Another intriguing possibility is spectroscopic variability. If there is only microlensing, then over the next few years image D ought to return to the brightness predicted by smooth lens models — in both the continuum and emission line. If there is any millilensing, then differences between observed and smooth model flux ratios will persist for centuries.

We are deeply grateful to Galina Soutchkova and David Solderblom at STScI for rescheduling our observations of SDSS0924 and supporting our request for ACS prism observations. We thank Chris Kochanek and the other members of HST program GO-9744 for arranging the direct ACS images. We thank A. Eigenbrod for communicating his measurement of the lens galaxy redshift prior to publication. We thank Frederic Courbin for valuable comments on the manuscript. We thank the referee, Prasenjit Saha, for constructive criticism and for helpful suggestions about the probability analysis. Support for HST program GO-9854 was provided by NASA through a grant from STScI, which is operated by the AURA, Inc., under NASA contract NAS 5-26555.

REFERENCES

- Bennert, N., Falcke, H., Schulz, H., Wilson, A. S., & Wills, B. J. 2002, *ApJ*, 574, L105
- Bolton, A. S., Burles, S., Koopmans, L. V. E., Treu, T., & Moustakas, L. A. 2005, in preparation
- Chang, K., & Refsdal, S. 1979, *Nature*, 282, 561
- Chiba, M. 2002, *ApJ*, 565, 17
- Chiba, M., Minezaki, T., Kashikawa, N., Kataza, H., & Inoue, K. T. 2005, *astro-ph/0503487*
- Dalal, N., & Kochanek, C. S. 2002, *ApJ*, 572, 25
- Eigenbrod, A., et al. 2005, *A&A*, submitted
- Inada, N., et al. 2003, *AJ*, 126, 666
- Kaspi, S., Moaz, D., Netzer, H., Peterson, B. M., Vestergaard, M., & Jannuzi, B. T. 2005, *astro-ph/0504484*
- Keeton, C. R., Gaudi, B. S., & Petters, A. O. 2003, *ApJ*, 598, 138
- Keeton, C. R., Gaudi, B. S., & Petters, A. O. 2005, *astro-ph/0503452*
- Keeton, C. R., Kochanek, C. S., & Seljak, U. 1997, *ApJ*, 482, 604
- Kochanek, C. S. 2002, in *The Shapes of Galaxies and Their Dark Matter Halos*, ed. P. Natarajan (Singapore: World Scientific), 62
- Kochanek, C. S. 2004, in *The Impact of Gravitational Lensing on Cosmology* (IAU 225), eds. Y. Mellier & G. Meylan; also *astro-ph/0412089*
- Kraemer, S. B., Crenshaw, D. M., Filippenko, A. V., & Peterson, B. M. 1998, *ApJ*, 499, 719
- Krist, J. 1995, *ASP Conference Series*, 77, 349
- Mao, S., & Schneider, P. 1998, *MNRAS*, 295, 587
- Metcalf, R. B., & Madau, P. 2001, *ApJ*, 563, 9
- Metcalf, R. B., Moustakas, L. A., Bunker, A. J., & Parry, I. R. 2004, *ApJ*, 607, 43
- Momcheva, I., Williams, K., Keeton, C., & Zabludoff, A. 2005, *ApJ*, submitted
- Mortonson, M. J., Schechter, P. L., & Wambsganss, J. 2005, *ApJ*, 628, 594
- Moustakas, L. A., & Metcalf, R. B. 2003, *MNRAS*, 339, 607
- Pavlovsky, C., et al. 2004, "ACS Instrument Handbook", Version 5.0, (Baltimore: STScI).
- Saha, P., & Williams, L. L. R. 2003, *AJ*, 125, 2769
- Schechter, P. L., & Wambsganss, J. 2002, *ApJ*, 580, 685
- Schechter, P. L., Wambsganss, J., & Lewis, G. F. 2004, *ApJ*, 613, 77
- Schneider, P., & Wambsganss, J. 1990, *A&A*, 237, 42
- Wambsganss, J. 1990a, PhD Thesis (Munich), also MPA report 550
- Wambsganss, J., Paczyński, B., & Schneider, P. 1990b, *ApJ*, 358, L33
- Wambsganss, J. 1999, *JCAM*, 109, 353
- Wayth, R. B., O'Dowd, M., & Webster, R. L. 2005, *MNRAS*, 359, 561
- Wisotzki, L., Becker, T., Christensen, L., Helms, A. Jahnke, K., Kelz, A., Roth, M. M., & Sanchez, S. F. 2003, *A&A*, 408, 455